Novel Compensation Method for Current Distortion in IPMSM with PWM Carrier-Synchronized Voltage Injection

Tetsuji Daido, *Member*, *IEEE*, Ryo Hisamatsu, Taisei Araki, and Shin-ichi Hamasaki, *Member, IEEE*

***Abstract*— A high-frequency signal voltage injection method synchronized with the carrier wave of pulse-width modulation (PWM) can be used to estimate the rotor position of interior permanent magnet synchronous motors (IPMSM) by the accompanying high-frequency current. In the signal voltage injection method, the sampled current differs from the actual instantaneous current at the instance of switching. However, the inverter output voltage error strongly depends on the output current amplitude and polarity. In this paper, we propose a method to compensate for the inverter output voltage error in each half of the PWM carrier period. Moreover, a technique for estimating the instantaneous current values based on the mathematical model of IPMSMs ensures that the proposed method can be combined with the signal voltage injection method. The proposed method was verified experimentally, and it resulted in a reduction in the low-order current distortion even when the output current has a large current ripple.**

***Index Terms*— carrier-synchronized signal voltage injection, dead time compensation, interior permanent magnet motor, pulse width modulation**

I. I. INTRODUCTION

INTERIOR permanent magnet synchronous motors (IPMSMs) have attracted increased research interest and are widely used because of their high efficiency, which is realized using permanent magnets with a strong magnetic field. To ensure high-efficiency adjustable speed operation, the inverter output current must be appropriately controlled based on the rotor position of the IPMSMs.

Position encoderless vector control has been studied in recent decades [1][2]. The back emf of IPMSMs is used to estimate the rotor position. However, the amplitude of the back emf is sufficiently small to distinguish it from the noise that occurs in the sensors when the rotating speed is low. Therefore, at a standstill or low speed, high-frequency signal voltages are injected to estimate the position by detecting the magnetic saliency of IPMSMs based on the corresponding currents extracted [3]–[11].

The currents generated by the injected high-frequency signal voltage are affected by the magnetic saliency of the IPMSMs; therefore, the currents extracted from the signal voltage enable the detection of the rotor position. There are two typical examples of signal voltages, namely the signal voltage synchronized with the carrier of the pulse width modulation (PWM) and the high-frequency signal current directly controlled by the modulated sinusoidal voltage. Carrier-synchronized signal voltage injection is advantageous in that no signal filter is required to extract the high-frequency signal current. The differentiated value of the precise current is obtained by utilizing synchronized current sampling. Therefore, precise synchronization between the carrier wave, signal voltage, and current sampling timing is crucial for accurate detection of the corresponding signal currents. A slight discrepancy in the timing between them can prevent precise signal current extraction [6]–[11].

This paper proposes an output voltage compensation method suitable for the carrier-synchronized signal voltage injection method. An important feature of the proposed method is that the output voltage error is compensated for in each half of the carrier period [11]–[13]. Compensating each half of the carrier period ensures that the average voltage error and the phase error of the modulated square-wave voltage are compensated for. The proposed compensation was carried out in a feedforward manner. To implement the proposed method, we developed a technique for measuring the output voltage errors in half of the carrier periods using a general-purpose microcontroller by sweeping the current command much slower than the time constant of the motor.

The signal voltage injection method generates a large current ripple whose period is that of the PWM carrier wave. However, the output voltage error strongly depends on the current amplitude and polarity, particularly close to zero ampere. The worst case is that the polarity of the sampled current is opposite that of the actual instantaneous current at the instance of switching, which reduces the accuracy of the output voltage compensation [10]–[20]. Therefore, this paper proposes a method for predicting the instantaneous current at the instance

Manuscript received. A short version of this manuscript was presented at the 2021 24th International Conference on Electrical Machines and Systems (DOI: 10.23919/ICEMS52562.2021.9634617).

The authors are with the Division of Electrical Engineering and Computer Science, Nagasaki University, Nagasaki 851-8521, Japan (e-mail: daido@nagasaki-u.ac.jp; hama-s@nagasaki-u.ac.jp).

Color versions of one or more of the figures in this article are available online at http://ieeexplore.ieee.org of switching instant, and the predicted current values were used for the proposed compensation method.

The proposed method for estimating the instantaneous current is based on the mathematical model of IPMSMs. Therefore, the mismatch between the mathematical model and an actual machine causes a current prediction error, which was not reported in the previous study [11]. Zero-current-clamping, which occurs during deadtime and current of zero ampere, is considered a serious factor that contributes to the current distortion, and it is difficult to compensate for this factor owing to current decay after switching [21]. In this study, a repetitive controller was introduced in the current control loop as a feedback-type output voltage error compensation method to avoid serious failure of the proposed output voltage error compensation [22]–[25]. The proposed methods were experimentally validated. The results demonstrate that the proposed method decreased the low-order current harmonic distortion even under a large current ripple.

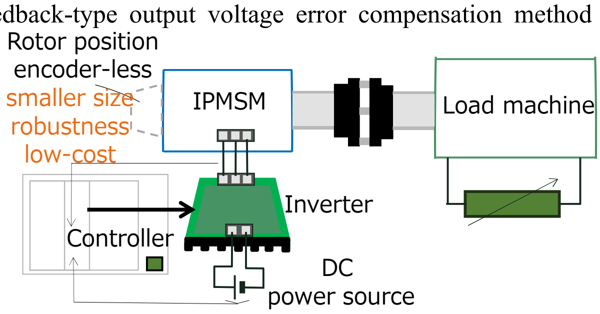

Fig. 1. Schematic of an experimental IPMSM drive system.

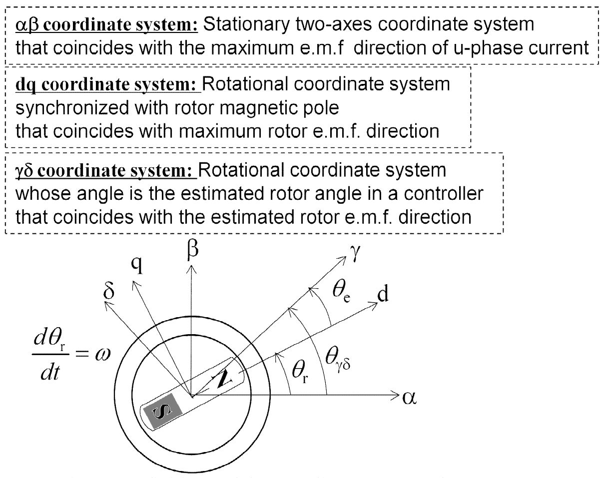

Fig. 2. Definitions of the coordinate systems for IPMSMs.

II. Carrier-Synchronized Signal Voltage Injection Method

A. Basic mathematical model for high-frequency voltage injection of IPMSMs

The high-frequency signal voltage injection method enables instantaneous torque control without a rotor position encoder. The signal voltage is injected using a PWM inverter directly connected to the IPMSM, as shown in Fig. 1. The rotor position is estimated based on the mathematical model of the IPMSMs. The definitions of the coordinate systems of IPMSMs are shown in Fig. 2. The overall control block diagram of the carrier-synchronized voltage method is shown in Fig. 3. The automatic speed and current regulators consist of digital proportional integral controllers. In Fig.3, all the proportional integral controllers in the discrete time domain are defined in the following equation, and their block diagram with anti-windup is depicted in Fig. 4.

$$Y(z)=z^{-1}Y(z)+k_{\mathrm{p}}\left(1-z^{-1}\right)E(z)+k_{\mathrm{i}}T_{\mathrm{s}}\frac{1+z^{-1}}{2}E(z), \quad (1)$$

where e is the input, y is the output, k_{p} is the proportional gain, k_{i} is the integral gain, T_{s} is the discrete interval, and z is the forward shift operator.

The equation of IPMSMs is given in instantaneous space vector representation as follows:

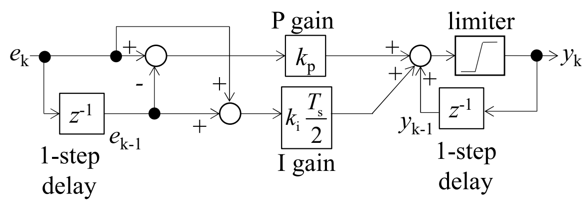

Fig. 4. Block diagram of a PI controller with an output limiter.

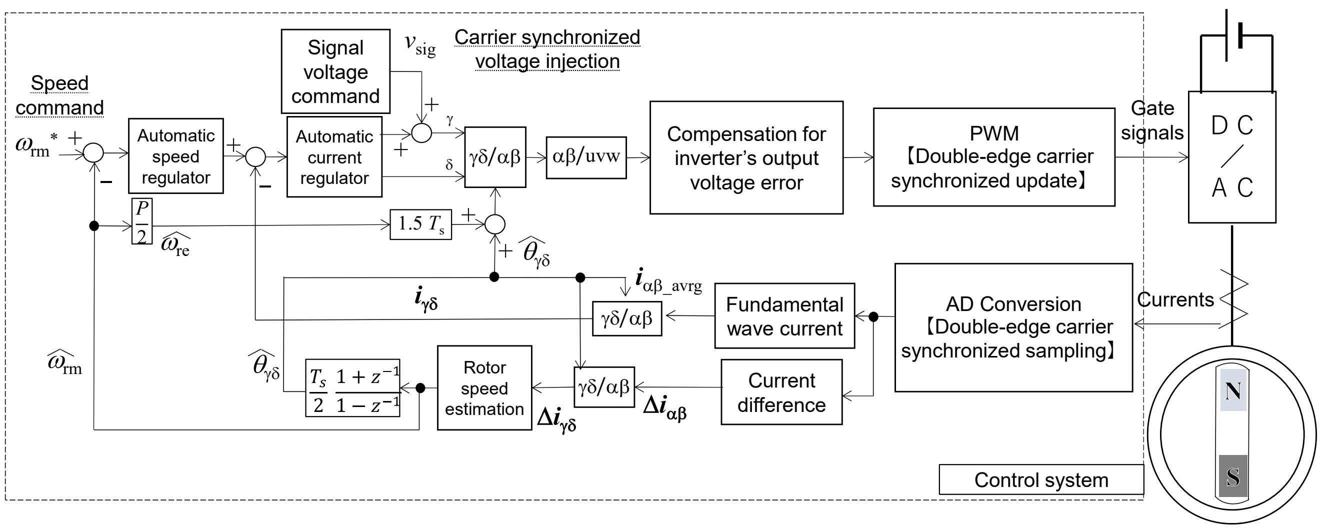

Fig. 3. Overall control block diagram of the carrier-synchronized voltage injection method.

$$\boldsymbol{v}_{\mathrm{dq}} = R_s\,\boldsymbol{i}_{\mathrm{dq}} + \left(\mathrm{p} + j\omega\right)\left(L_{\mathrm{d}}\, i_{\mathrm{d}} + \psi + j\, L_{\mathrm{q}}\, i_{\mathrm{q}}\right), \qquad (2)$$

where R_s is the stator resistance, ω is the synchronous angular frequency in electrical angle, L_d and L_q are the stator self-inductances, Ψ is the flux linkage of the permanent magnet, $\boldsymbol{v}_{dq}$ is the stator voltage, and $\boldsymbol{i}_{dq}$ is the stator current space vector, which can be divided into $i_d + j\, i_q$. This equation is transformed into the γδ coordinate system by multiplying (1) by exp $(-j\ \theta_e)$, as follows:

$$\begin{aligned}\boldsymbol{v}_{\gamma\delta} &= R_s\,\boldsymbol{i}_{\gamma\delta} + \left(\mathrm{p} + j\omega\right)\\ &\quad \left[\left\{\left(L_0 - L_1\cos 2\theta_{\mathrm{e}}\right) i_\gamma + \left(L_1 \sin 2\theta_{\mathrm{e}}\right) i_\delta\right\}\right. \\ &\quad \left. + j\left\{\left(L_1 \sin 2\theta_{\mathrm{e}}\right) i_\gamma + \left(L_0 + L_1\cos 2\theta_{\mathrm{e}}\right) i_\delta\right\}\right] \\ &\quad + j e^{-j\theta_{\mathrm{e}}}\omega\psi\end{aligned}, \qquad (3)$$

where L_0 is $(L_d + L_q)/2$, and L_1 is $(L_q - L_d)/2$. This equation is expanded to transpose the time derivative term to the left-hand side.

$$\begin{aligned}\mathrm{p}\boldsymbol{i}_{\gamma\delta} &= \frac{L_{\mathrm{d}} + L_{\mathrm{q}}}{2L_{\mathrm{d}}L_{\mathrm{q}}}\left\{\boldsymbol{v}_{\gamma\delta} - \left(R_s + j\omega\left(L_{\mathrm{d}} + L_{\mathrm{q}}\right)\right)\boldsymbol{i}_{\gamma\delta}\right\} \\ &\quad + \frac{L_{\mathrm{q}} - L_{\mathrm{d}}}{2L_{\mathrm{d}}L_{\mathrm{q}}}\overline{e^{j2\theta_{\mathrm{e}}}}\left\{\overline{\boldsymbol{v}_{\gamma\delta}} - \overline{\left(R_s + j\omega\left(L_{\mathrm{d}} + L_{\mathrm{q}}\right)\right)\boldsymbol{i}_{\gamma\delta}}\right\} \\ &\quad + j\omega\left(\boldsymbol{i}_{\gamma\delta} - \frac{\psi}{L_{\mathrm{d}}}e^{-j\theta_{\mathrm{e}}}\right)\end{aligned}, \qquad (4)$$

where the upper bar indicates the conjugate complex number. If only the high-frequency signal voltage is considered in (4), the terms that have $\boldsymbol{v}_{\gamma\delta}$ on the right-hand side of the equation are dominant because the amplitude of the signal voltage is large; then, the following equation is obtained.

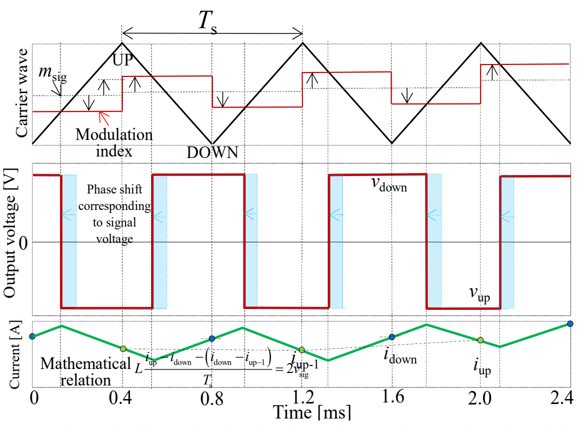

Fig. 5. Schemati of how the signal voltage is superimposed on the original modulation index and affects the high-frequency current.

$$\mathrm{p}\boldsymbol{i}_{\gamma\delta} = \frac{L_{\mathrm{d}} + L_{\mathrm{q}}}{2L_{\mathrm{d}}L_{\mathrm{q}}} v_{\mathrm{sig}}{}^{*} + \frac{L_{\mathrm{q}} - L_{\mathrm{d}}}{2L_{\mathrm{d}}L_{\mathrm{q}}} e^{-j2\theta_{\mathrm{e}}} v_{\mathrm{sig}}{}^{*}. \qquad (5)$$

The injection voltage command $v_{sig}{}^{*}$ shifts the phase of the modulated square wave voltage, as illustrated in Fig. 5. The difference in the current from the up to the previous down timings of the carrier wave $\Delta\boldsymbol{i}_{1\gamma\delta}$ is derived as follows:

$$\Delta\boldsymbol{i}_{1\gamma\delta} = \left(\frac{L_{\mathrm{d}} + L_{\mathrm{q}}}{2L_{\mathrm{d}}L_{\mathrm{q}}} + \frac{L_{\mathrm{q}} - L_{\mathrm{d}}}{2L_{\mathrm{d}}L_{\mathrm{q}}} e^{-j2\theta_{\mathrm{e}}}\right) v_{\mathrm{sig}}{}^{*}\frac{T_{\mathrm{s}}}{2}. \qquad (6)$$

Similarly, the difference in the current from the down to the previous up timings of the carrier wave $\Delta\boldsymbol{i}_{2\gamma\delta}$ is derived as follows:

$$\Delta\boldsymbol{i}_{2\gamma\delta} = -\left(\frac{L_{\mathrm{d}} + L_{\mathrm{q}}}{2L_{\mathrm{d}}L_{\mathrm{q}}} + \frac{L_{\mathrm{q}} - L_{\mathrm{d}}}{2L_{\mathrm{d}}L_{\mathrm{q}}} e^{-j2\theta_{\mathrm{e}}}\right) v_{\mathrm{sig}}{}^{*}\frac{T_{\mathrm{s}}}{2}. \qquad (7)$$

The two current space vectors are subtracted to obtain

$$\Delta\boldsymbol{i}_{\gamma\delta} = \Delta\boldsymbol{i}_{1\gamma\delta} - \Delta\boldsymbol{i}_{2\gamma\delta} = \frac{v_{\mathrm{sig}}{}^{*}}{L_{\mathrm{d}}L_{\mathrm{q}}}\frac{T_{\mathrm{s}}}{2}\left\{L_{\mathrm{d}} + L_{\mathrm{q}} + \left(L_{\mathrm{q}} - L_{\mathrm{d}}\right)e^{-j2\theta_{\mathrm{e}}}\right\}. \qquad (8)$$

The differential current space vector is decomposed into the scalar values as follows:

$$\Delta i_\gamma = \frac{v_{\mathrm{sig}}{}^{*}}{L_{\mathrm{d}}L_{\mathrm{q}}}\frac{T_{\mathrm{s}}}{2}\left\{L_{\mathrm{d}} + L_{\mathrm{q}} + \left(L_{\mathrm{q}} - L_{\mathrm{d}}\right)\cos 2\theta_{\mathrm{e}}\right\}, \qquad (9)$$

$$\Delta i_\delta = -\frac{v_{\mathrm{sig}}{}^{*}}{L_{\mathrm{d}}L_{\mathrm{q}}}\frac{T_{\mathrm{s}}}{2}\left(L_{\mathrm{q}} - L_{\mathrm{d}}\right)\sin 2\theta_{\mathrm{e}}. \qquad (10)$$

The error in the estimated rotor angle θ_e converges to zero when Δi_δ is controlled to zero, as given in (10). Fig. 6 shows the experimental results for the high-frequency current against the signal voltage. A six-pole IPMSM was used as the test motor, and hence, there are six specific rotor angles where the estimated angle converges because the phase angle of the high-frequency current is zero. Magnetic polarity judgement was executed at startups to ensure that it converges to the N magnetic pole's position.

B. Independent control method for average currents and PWM ripple currents in the PWM carrier period

The sampled currents are composed of the fundamental wave component as well as the ripple current component inherently generated by PWM. In particular, when the signal voltage injection method is used, accurate sampling of the fundamental wave current is difficult because of the additional ripple currents by the signal voltage, as illustrated in Fig. 5. In this study, the average currents $\boldsymbol{i}_{\alpha\beta\_avrg}$ and ripple currents $\Delta\boldsymbol{i}_{\alpha\beta}$ in the αβ stationary coordinate system were calculated at every up

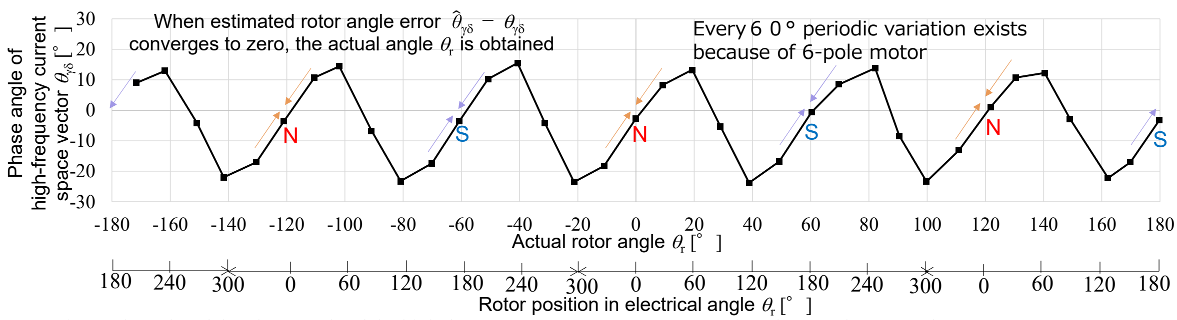

Fig. 6. Experimental results of the phase angle of the high-frequency current space vector against the actual rotor angle.

timing of the PWM carrier wave, as given in the following equations:

$$\boldsymbol{i}_{\alpha\beta\_\mathrm{avrg}} = \frac{\left(\boldsymbol{i}_{\alpha\beta\_\mathrm{up}} + 2\,\boldsymbol{i}_{\alpha\beta\_\mathrm{down}} + \boldsymbol{i}_{\alpha\beta\_\mathrm{up\text{-}1}}\right)}{4}, \tag{11}$$

$$\Delta\boldsymbol{i}_{\alpha\beta} = \left(\boldsymbol{i}_{\alpha\beta\_\mathrm{up}} - \boldsymbol{i}_{\alpha\beta\_\mathrm{down}}\right) - \left(\boldsymbol{i}_{\alpha\beta\_\mathrm{down}} - \boldsymbol{i}_{\alpha\beta\_\mathrm{up\text{-}1}}\right). \tag{12}$$

The phase angles of the average currents $\boldsymbol{i}_{\alpha\beta\_\mathrm{avrg}}$ and ripple currents $\Delta\boldsymbol{i}_{\alpha\beta}$ equivalently coincide with the down edge timings of the PWM carrier wave.

C. *Estimation of rotor speed and position using δ-axis differential current*

Position estimation must be performed regardless of the level of noise in the δ-axis differential current. Therefore, the rotor speed and position were estimated such that the effect of noise is minimized. A high-order phase-locked loop to estimated them was constructed for noise rejection to estimate these parameters [26].

The open-loop transfer function from Δi_δ to $\theta_{\gamma\delta}$ is as follows:

$$\frac{\theta_{\gamma\delta}}{\Delta i_\delta} = \frac{1}{s}\left\{ l_1 + \frac{1}{s}\left(l_2 + \frac{l_3}{J}\frac{1}{s} \right) \right\}. \tag{13}$$

If Δi_δ has a monotonically increasing relationship with the estimated angle error θ_e, the block diagram in which the angle error converges to zero is depicted in Fig. 7, and the closed-loop transfer function is obtained as follows:

$$\frac{\theta_{\gamma\delta}}{\theta_r} = \frac{l_1 s^2 + l_2 s + \dfrac{l_3}{J}}{s^3 + l_1 s^2 + l_2 s + \dfrac{l_3}{J}} = \frac{3\alpha s^2 + 3\alpha^2 s + \alpha^3}{(s+\alpha)^3}. \tag{14}$$

The poles were set to be a triple root whose value α is 500/3 rad/s (28 Hz) in this study. Subsequently, all zeros are allocated to the negative real region.

III. Rotor Position Estimation Error

Accurate estimation of the rotor's maximum magnetomotive force position yields the maximum output torque per stator current. However, this estimation inevitably leads to an error. Signal voltage injection methods produce an estimation error, depending on the operating conditions. Some sources of the estimation error, which have been addressed in existing studies, are listed below.

- Magnetic saturation and d-q magnetic path coupling
- Non-sinusoidal magnetic flux distribution
- Estimation delay in high-speed rotating operation
- Insufficiently accurate sensor resolution to detect the signal currents
- Inverter's output voltage errors

The effects of the nonideal magnetic characteristics and structure of the machine have been reported in the literatures. Although inverter output voltage error compensation is necessary to reduce the estimation error and output torque fluctuation, few papers have reported on the compensation method suitable for the signal voltage injection method.

IV. Output Voltage Error Compensation for the Signal Voltage Injection Method

In the signal voltage injection method, the increase in the current ripple is large. As a result, the current polarity detection is difficult, and may not compensate the output voltage error. Therefore, this paper proposed that the inverter output voltage error should be compensated for in each half period of the PWM carrier wave. To implement the proposed method, we developed an instantaneous current prediction method at the switching timings.

First, the inverter output voltage error measurement while keeping the three-phase wires connected to the motor is explained.

A. *Measurement of the output voltage error*

The output voltage error was measured, without any special equipment, by sweeping the current command i^* much slower than the time constant of the motor, as given in the following equations.

$$\begin{aligned} i_u^* &= i^* \\ i_v^* &= I^* - \frac{i^*}{2} \\ i_w^* &= -I^* - \frac{i^*}{2} \end{aligned}, \tag{15}$$

where i^* is the current command at the measured phase and I^* is the relatively large current amplitude value (3.5 A) to avoid changing the current polarity at the remaining two phases. The current command is swept according to the following equation.

$$i^* = I_{\mathrm{sweep}} \sin^3\left(\frac{2\pi}{T_{\mathrm{sweep}}} t\right), \tag{16}$$

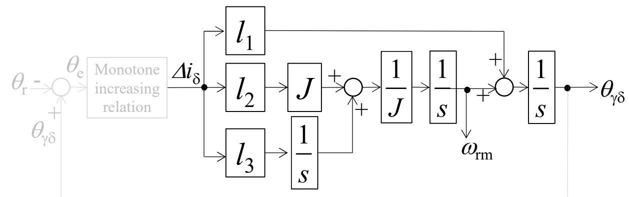

Fig. 7. Block diagram for estimating the rotor angle and position using the current difference in the δ-axis.

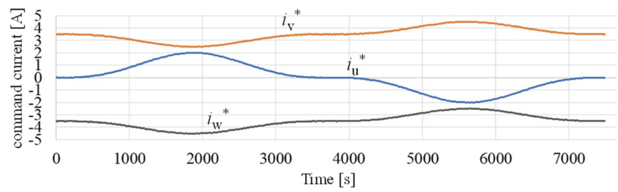

Fig. 8. Sweeping current commands for measuring the output voltage error.

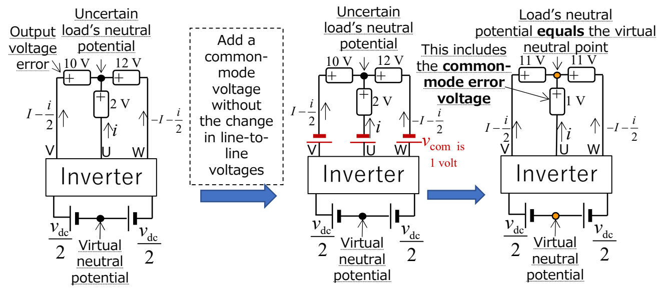

Fig. 9. Example of measurement of error voltage including the common-mode component.

where T_{sweep} was set to 7500 s (approximately 2 h) to eliminate the voltage drop at the inductances of the motor. The current command waveforms are shown in Fig. 8.

If a three-phase inverter is connected to a motor, the common-mode voltage has one degree of freedom. Therefore, an accurate phase voltage error cannot be detected. To accurately measure the phase voltage error, the virtual neutral point potential of the dc side voltage of an inverter is made equal to the load neutral point potential by feeding the same voltage amplitude with opposite polarity at the rest of the two phases, as illustrated in Fig. 9.

The phase error of the modulated voltage and current deviation between the up and down timings of the carrier wave is illustrated in Fig. 10. A control block diagram of the output voltage error measurement in the carrier half period is shown in Fig. 11. The proportional gain k_p and integral gain k_i for the average current control were set to 0.1 and 1000, respectively. The output voltage command for the u-phase average current control is expressed by the following equation.

$$v_{u\_avrg}^{*} = \left(k_p + k_i \frac{T_s}{2}\frac{1+z^{-1}}{1-z^{-1}}\right)\left(i_u^{*} - \frac{i_{u\_up} + 2i_{u\_down} + i_{u\_up-1}}{4}\right), \quad (17)$$

$$v_{u\_ripple}^{*} = \left(k_{rp} + k_i \frac{T_s}{2}\frac{1+z^{-1}}{1-z^{-1}}\right)\left\{\left(i_{u\_up} - i_{u\_down}\right) - \left(i_{u\_down} - i_{u\_up-1}\right)\right\}. \quad (18)$$

Only the phase correction was implemented at the phase where the output voltage error was measured. Then, each up and down of the output voltage command is expressed as follows:

$$v_{u\_up}^{*} = v_{u\_avrg}^{*} + v_{u\_ripple}^{*} + R_s i_u^{*}, \quad (19)$$

$$v_{u\_down}^{*} = v_{u\_avrg}^{*} - v_{u\_ripple}^{*} + R_s i_u^{*}. \quad (20)$$

A PI controller was used to correct the phase angle of the square wave output voltage, whose gain k_{rp} was set to 0.001. The proportional gain was set to a small value to avoid sensor noise, whereas the integral gain was set to a large value to eliminate steady error. The integral gain k_{ri} was obtained by the mathematical equation of ripple current control as follows:

$$\left(\Delta i_u - \Delta i_u^{*}\right) z^{-1} k_{ri} \frac{1+z^{-1}}{1-z^{-1}}\frac{T_s}{2} = L\frac{1-z^{-1}}{T_s}\Delta i_u + R_s \frac{1+z^{-1}}{2}\Delta i_u. \quad (21)$$

The equation is expanded as follows:

$$\frac{\Delta i_u}{\Delta i_u^{*}} = \frac{(z+1) k_{ri} T_s}{(z+1) k_{ri} T_s + 2\frac{L}{T_s}(z-1)^2 + R_s\left(z^2 - 1\right)}. \quad (22)$$

The magnitude of the closed poles must be within a unit circle so that the control system is stable. The poles are obtained as follows:

$$z = \frac{\left(4\frac{L}{T_s} - k_{ri} T_s\right) \pm \sqrt{T_s^2 (k_{ri})^2 - (16L + 4R_s T_s) k_{ri} + 4R_s^2}}{2\left(2\frac{L}{T_s} + R_s\right)}. \quad (23)$$

In our experimental setup, the values of k_{ri} are 52 and 154698 when the magnitude of the poles is 1. In this study, we selected an integral gain of 10000 considering this stability margin.

Fig. 12 shows the measured average output voltage errors

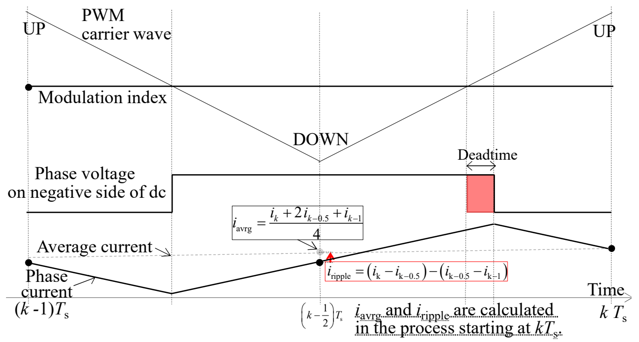

Fig. 10. Example of how an average current i_{avrg} and a phase error current i_{ripple} appear.

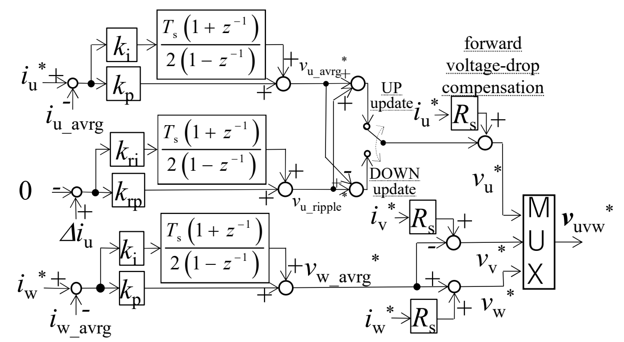

Fig. 11. Block diagram for error voltage measurement in half the carrier period.

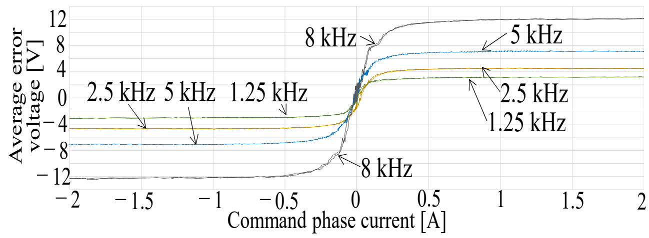

Fig. 12. Average error voltage against current and carrier frequency.

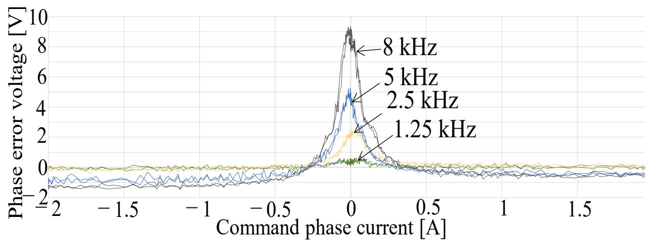

Fig. 13. Phase error voltage against current and carrier frequency.

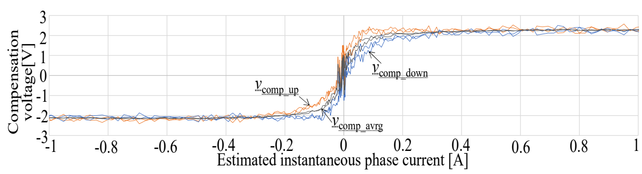

Fig. 14. Compensation voltage against instantaneous phase current at a carrier frequency of 1.25 kHz.

$v_{u\_avrg}^{*}$ with respect to the phase current amplitude. The carrier frequencies are also shown in the figure. The measured errors were excluded by ohmic and forward voltage drops after processing the measured results [13]. The figure clearly shows the abrupt voltage error change in the vicinity of zero ampere. In contrast, the average error voltage is proportional to the PWM carrier frequency when the phase current is large. Fig. 13 shows the phase correction voltage $v_{u\_ripple}^{*}$ with respect to the phase current. When the carrier frequency increases, the voltage is clearly visible compared with that at a lower frequency. Fig. 14 shows the feedforward compensation voltages v_{comp_up} and v_{comp_down} calculated from (19) and (20) at a carrier frequency of 1.25 kHz. Because of the low carrier frequency, the difference between v_{comp_up} and v_{comp_down} is small.

B. Instantaneous current prediction for IPMSM

The ripple current is particularly large for carrier-synchronized signal voltage injection, which makes output voltage error compensation difficult. In this study, a method for estimating the instantaneous ripple current was established to improve the accuracy of the proposed compensation.

Fig. 15 illustrates how the output voltage space vector changes during the period of the PWM carrier wave [28]. In this signal voltage injection method, the modulation indices are updated at the double edges of the carrier wave. Variables *a*, *b*, and *c* indicate the time ratio in terms of the carrier interval, which has the following relationship.

$$\frac{a_{up}+a_{down}}{2}+\frac{b_{up}+b_{down}}{2}+\frac{c_{up}+c_{down}}{2}=1. \tag{24}$$

Fig. 16 shows the fundamental wave output voltage vectors. If the time of the first up timing in the figure is assumed, the time lapses illustrated in Fig. 15 can be calculated as follows:

$$t_1=\frac{c_{up}}{4}T_s,\ t_2=\left(\frac{c_{up}}{4}+\frac{a_{up}}{2}\right)T_s,\ t_3=\left(\frac{c_{up}}{4}+\frac{a_{up}}{2}+\frac{b_{up}}{2}\right)T_s,$$

$$t_4=\left(\frac{1}{2}+\frac{c_{down}}{4}\right)T_s,\ t_5=\left(\frac{1}{2}+\frac{c_{down}}{4}+\frac{b_{down}}{2}\right)T_s,$$

$$t_6=\left(\frac{1}{2}+\frac{c_{down}}{4}+\frac{b_{down}}{2}+\frac{a_{down}}{2}\right)T_s.$$

In Fig. 15, $\boldsymbol{V}_a$ is the fundamental output voltage space vector whose positive phase voltage is larger than that of $\boldsymbol{V}_b$, which is explained later. Fig. 16 shows the possible voltage vector of a two-level three-phase inverter. Because of the three-phase and two-level inverters, the number of possible voltage vectors $\boldsymbol{V}_a$ is three, which are written in underlined bold font. The fundamental output voltage space vector $\boldsymbol{V}_b$ indicates that the negative phase voltage is smaller than that of $\boldsymbol{V}_a$. The average voltages in a single carrier interval are expressed as follows:

$$\overline{\boldsymbol{v}_{up}}=a_{up}\boldsymbol{V}_{aup}-b_{up}\boldsymbol{V}_{bup}, \tag{25}$$

$$\overline{\boldsymbol{v}_{down}}=a_{down}\boldsymbol{V}_{adown}-b_{down}\boldsymbol{V}_{bdown}, \tag{26}$$

where the upper bar indicates the average value for one PWM carrier period. The average output voltage during the carrier period is expressed as

$$\begin{aligned}\overline{\boldsymbol{v}_{\alpha\beta}}&=\frac{\overline{\boldsymbol{v}_{up}}+\overline{\boldsymbol{v}_{down}}}{2}\\&=\frac{a_{up}\boldsymbol{V}_{aup}+a_{down}\boldsymbol{V}_{adown}}{2}-\frac{b_{up}\boldsymbol{V}_{bup}+b_{down}\boldsymbol{V}_{bdown}}{2}\end{aligned}. \tag{27}$$

Here, the following variables are introduced to simplify (27):

$$\overline{\boldsymbol{v}_{\alpha\beta}}=a_{avrg}\boldsymbol{V}_{aavrg}-b_{avrg}\boldsymbol{V}_{bavrg}. \tag{28}$$

A virtual ripple flux space vector is defined as follows:

$$\Delta\boldsymbol{\lambda}_{\alpha\beta}(t)=\int_0^t\left(\boldsymbol{v}_{\alpha\beta}-\overline{\boldsymbol{v}_{\alpha\beta}}\right)dt=\int_0^t\Delta\boldsymbol{v}_{\alpha\beta}\,dt. \tag{29}$$

The ripple voltage space vectors $\Delta\boldsymbol{v}_{\alpha\beta}$ are listed in Table I. The flux space vector is transformed into the dq coordinate system as follows:

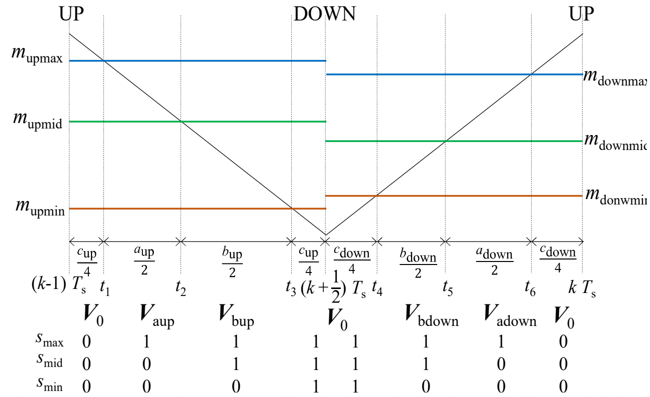

Fig. 15. Output voltage vector for double-edge updates of the modulation index for the carrier-synchronized signal voltage injection.

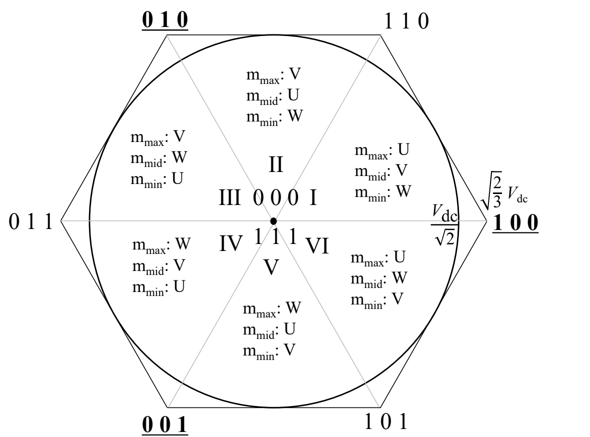

Fig. 16. Sectors of the inverter output voltage vectors on the αβ stationary reference system.

TABLE I RIPPLE VOLTAGE SPACE VECTORS $\Delta\boldsymbol{v}_{\alpha\beta}$

Time sector	Duration ratio	Ripple voltage
$0 \leqq t \leqq t_1$	$c_{up}/4$	$-a_{avrg}\boldsymbol{V}_{aavrg}+b_{avrg}\boldsymbol{V}_{bavrg}$
$t_1 \leqq t \leqq t_2$	$a_{up}/2$	$\boldsymbol{V}_{aup}-a_{avrg}\boldsymbol{V}_{aavrg}+b_{avrg}\boldsymbol{V}_{bavrg}$
$t_2 \leqq t \leqq t_3$	$b_{up}/2$	$-\boldsymbol{V}_{bup}-a_{avrg}\boldsymbol{V}_{aavrg}+b_{avrg}\boldsymbol{V}_{bavrg}$
$t_3 \leqq t \leqq T_s/2$	$c_{up}/4$	$-a_{avrg}\boldsymbol{V}_{aavrg}+b_{avrg}\boldsymbol{V}_{bavrg}$
$T_s/2 \leqq t \leqq t_4$	$c_{down}/4$	$-a_{avrg}\boldsymbol{V}_{aavrg}+b_{avrg}\boldsymbol{V}_{bavrg}$
$t_4 \leqq t \leqq t_5$	$b_{down}/2$	$-\boldsymbol{V}_{bdown}-a_{avrg}\boldsymbol{V}_{aavrg}+b_{avrg}\boldsymbol{V}_{bavrg}$
$t_5 \leqq t \leqq t_6$	$a_{down}/2$	$\boldsymbol{V}_{adown}-a_{avrg}\boldsymbol{V}_{aavrg}+b_{avrg}\boldsymbol{V}_{bavrg}$
$t_6 \leqq t \leqq T_s$	$c_{down}/4$	$-a_{avrg}\boldsymbol{V}_{aavrg}+b_{avrg}\boldsymbol{V}_{bavrg}$

$$\lambda_{\mathrm{dq}} = L_{\mathrm{d}}\, i_{\mathrm{d}} + j\, L_{\mathrm{q}}\, i_{\mathrm{q}} . \tag{30}$$

The time derivative is calculated as follows:

$$\mathrm{p}\lambda_{dq} = L_{\mathrm{d}}\, \mathrm{p}i_{\mathrm{d}} + j\, L_{\mathrm{q}}\, \mathrm{p}i_{\mathrm{q}} = \mathrm{e}^{-j\theta_{\mathrm{r}}}\left(\mathrm{p} - j\omega\right)\lambda_{\alpha\beta} . \tag{31}$$

Assuming that $\mathrm{p}\lambda_{\alpha\beta}$ is much larger than $\omega\, \lambda_{\alpha\beta}$, the equation can be simplified as

$$L_{\mathrm{d}}\, \mathrm{p}i_{\mathrm{d}} + j\, L_{\mathrm{q}}\, \mathrm{p}i_{\mathrm{q}} = \mathrm{e}^{-j\theta_{\mathrm{r}}}\, \mathrm{p}\lambda_{\alpha\beta} . \tag{32}$$

The high-frequency ripple currents are derived as follows:

$$\Delta i_{\mathrm{d}} = \frac{1}{L_{\mathrm{d}}} \mathrm{Re}\left[\exp^{-j\theta_{\mathrm{r}}}\, \Delta\lambda_{\alpha\beta}\right] = \frac{1}{L_{\mathrm{d}}}\left(\Delta\lambda_{\alpha}\cos\theta_{\mathrm{r}} + \Delta\lambda_{\beta}\sin\theta_{\mathrm{r}}\right), \tag{33}$$

$$\Delta i_{\mathrm{q}} = \frac{1}{L_{\mathrm{q}}} \mathrm{Im}\left[\exp^{-j\theta_{\mathrm{r}}}\, \Delta\lambda_{\alpha\beta}\right] = \frac{1}{L_{\mathrm{q}}}\left(-\Delta\lambda_{\alpha}\sin\theta_{\mathrm{r}} + \Delta\lambda_{\beta}\cos\theta_{\mathrm{r}}\right). \tag{34}$$

The ripple currents in the dq coordinate system are transformed into the αβ coordinate system as follows:

$$\begin{aligned}
\Delta \boldsymbol{i}_{\alpha\beta} &= \mathrm{e}^{j\theta_{\mathrm{r}}}\, \Delta \boldsymbol{i}_{\mathrm{dq}} \\
&= \frac{1}{L_{\mathrm{d}}}\left(\Delta\lambda_{\alpha}\frac{1+\cos 2\theta_{\mathrm{r}}}{2} + \Delta\lambda_{\beta}\frac{\sin 2\theta_{\mathrm{r}}}{2}\right) \\
&\quad - \frac{1}{L_{\mathrm{q}}}\left(\Delta\lambda_{\alpha}\frac{1-\cos 2\theta_{\mathrm{r}}}{2} + \Delta\lambda_{\beta}\frac{\sin 2\theta_{\mathrm{r}}}{2}\right) \\
&\quad + j\left\{\frac{1}{L_{\mathrm{d}}}\left(\Delta\lambda_{\alpha}\frac{\sin 2\theta_{\mathrm{r}}}{2} + \Delta\lambda_{\beta}\frac{1-\cos 2\theta_{\mathrm{r}}}{2}\right) \right. \\
&\quad \left. + \frac{1}{L_{\mathrm{q}}}\left(-\Delta\lambda_{\alpha}\frac{\sin 2\theta_{\mathrm{r}}}{2} + \Delta\lambda_{\beta}\frac{1+\cos 2\theta_{\mathrm{r}}}{2}\right)\right\}
\end{aligned} . \tag{35}$$

The three-phase ripple currents are expressed as follows:

$$\Delta i_{\mathrm{u}} = \sqrt{\frac{2}{3}}\mathrm{Re}\left[\Delta \boldsymbol{i}_{\alpha\beta}\right] = \sqrt{\frac{2}{3}}\Delta i_{\alpha}, \tag{36}$$

$$\Delta i_{\mathrm{v}} = \sqrt{\frac{2}{3}}\mathrm{Re}\left[e^{-j\frac{2}{3}\pi}\Delta \boldsymbol{i}_{\alpha\beta}\right] = \sqrt{\frac{2}{3}}\left(-\frac{1}{2}\Delta i_{\alpha} + \frac{\sqrt{3}}{2}\Delta i_{\beta}\right), \tag{37}$$

$$\Delta i_{\mathrm{w}} = \sqrt{\frac{2}{3}}\mathrm{Re}\left[e^{j\frac{2}{3}\pi}\Delta \boldsymbol{i}_{\alpha\beta}\right] = \sqrt{\frac{2}{3}}\left(-\frac{1}{2}\Delta i_{\alpha} - \frac{\sqrt{3}}{2}\Delta i_{\beta}\right). \tag{38}$$

In the above equations, the amplitude of the ripple current becomes zero at the up edge timing of the carrier wave. On the contrary, the ripple current at the down edge timing of the carrier wave is derived based on (29). The ripple flux is expressed as follows:

$$\Delta\lambda_{\alpha\beta}\left(\frac{T_{\mathrm{s}}}{2}\right) = \left(\frac{a_{\mathrm{up}}V_{\mathrm{aup}} - a_{\mathrm{avrg}}V_{\mathrm{aavrg}}}{2} - \frac{b_{\mathrm{up}}V_{\mathrm{bup}} - b_{\mathrm{avrg}}V_{\mathrm{bavrg}}}{2}\right)T_{\mathrm{s}} . \tag{39}$$

The corresponding ripple currents are derived and expressed as $\Delta i_{\mathrm{u\_down}}$, $\Delta i_{\mathrm{v\_down}}$, and $\Delta i_{\mathrm{w\_down}}$. The average ripple currents are then derived by subtracting half of $\Delta i_{\mathrm{\_down}}$ from the estimated ripple currents. Consequently, the instantaneous currents i_{comp} for output voltage compensation are expressed as follows:

$$i_{\mathrm{u\_comp}} = i_{\mathrm{u\_avrg}} + \Delta i_{\mathrm{u}} - 0.5\,\Delta i_{\mathrm{u\_down}} , \tag{40}$$

$$i_{\mathrm{v\_comp}} = i_{\mathrm{v\_avrg}} + \Delta i_{\mathrm{v}} - 0.5\,\Delta i_{\mathrm{v\_down}} , \tag{41}$$

$$i_{\mathrm{w\_comp}} = i_{\mathrm{w\_avrg}} + \Delta i_{\mathrm{w}} - 0.5\,\Delta i_{\mathrm{w\_down}} . \tag{42}$$

The compensation voltages in both the first half of the carrier period (up to down tips of the carrier wave) and the second half were calculated at the up edge timing of the carrier wave.

C. Output voltage error compensation in the half of the carrier period

The compensation voltages were updated at both the up and down edges of the carrier wave, and the compensation voltages at both edge timings were calculated at the up edges of the carrier wave. The measured error voltages shown in Figs. 12 and 13 were approximated using polynomial equations as a function of the sampled current during commissioning. The compensation voltages were normalized by half of the DC voltage. These voltages were then added to the original modulation indices.

D. Feedback compensation for the current distortion

Because the output voltage error differs in each leg, feedback compensation of the output voltage distortion is necessary to limit variations in the output voltage error.

The ideal output voltage error V_{dead} of a leg as a result of a dead time insertion is expressed as follows:

$$V_{\mathrm{dead}} = \frac{T_{\mathrm{dead}}}{T_{\mathrm{s}}} V_{\mathrm{dc}}\, \mathrm{sgn}\left(i_{\mathrm{x}}\right) . \tag{43}$$

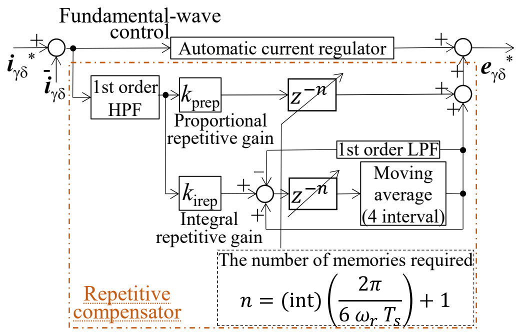

Fig. 17. Repetitive compensator for removing periodic current distortion.

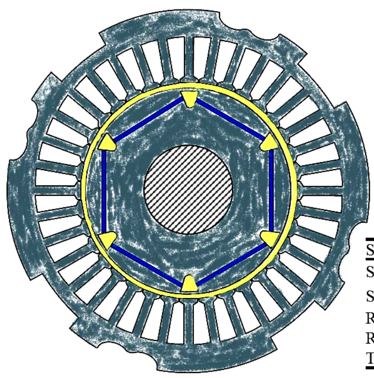

Size of the motor's core	Unit
Stator outer diameter	122.7mm
Stator inner diameter	72.5 mm
Rotor diameter	69.7 mm
Rotor shaft diameter	30 mm
Thickness of a core stack	180 mm

Fig. 18. Cross-section of the test IPMSM iron core.

TABLE II PARAMETERS OF THE TEST IPMSM

Rated			Nominal parameters		
Rated	750	W	Stator resistance R_{s}	1.132	Ω
Pole and slot	6 / 36	pole slot	d-axis stator self-inductance L_{d}	12.38	mH
Voltage	153	V	q-axis stator self-inductance L_{q}	15.72	mH
Frequency	87.5	Hz	Permanent magnet flux linkage Ψ	0.266	Wb
Current	3.4	A	Inertia J	6.0	10^{-3} kg m^2

The three-phase inverter generates the following space vector error voltage on the αβ stationary coordinate system.

$$\Delta \boldsymbol{v}_{\alpha\beta\mathrm{dead}} = \sqrt{\frac{3}{2}}\frac{4V_{\mathrm{dead}}}{\pi}\left(e^{j\theta} + \sum_{n=6k-1}^{\infty}\frac{1}{n}e^{-jn\theta} - \sum_{n=6k+1}^{\infty}\frac{1}{n}e^{jn\theta}\right), \quad (44)$$

where θ represents the current phase angle rotating at the fundamental angular frequency of ω_r and k is a positive integer. The error voltage space vector is transformed into the γδ coordinate system

$$\Delta \boldsymbol{v}_{\gamma\delta\mathrm{dead}} = \sqrt{\frac{3}{2}}\frac{4V_{\mathrm{dead}}}{\pi}e^{j\gamma}\left(1 + \sum_{n=6k}^{\infty}\frac{1}{n-1}e^{-jn(\theta_{\gamma\delta}+\gamma)} - \sum_{n=6k}^{\infty}\frac{1}{n+1}e^{jn(\theta_{\gamma\delta}+\gamma)}\right), \quad (45)$$

where γ is $\theta - \theta_{\gamma\delta}$. The error voltage changes periodically at a multiple of six times the fundamental wave angular frequency of ω_r. Therefore, the repetitive current distortion compensator proposed in [22]–[25], whose period was set to six times the period of ω_r, was added in parallel to the current controller, as shown in Fig. 17. The repetitive gains k_{prep} and k_{irep} were determined by trial and error.

V. Experimental Results

The proposed output voltage error compensation method suitable for high-frequency signal voltage injection was experimentally verified. The initial rotor position was estimated beforehand by detecting the current peak when a pulse voltage was applied [29][30].

A. Experimental setups

The IPMSM used in the test is a commercially available unit, with a rated power of 0.7 kW. The cross-section of the motor is shown in Fig. 18. The specifications and rated values of the motor are summarized in Table II. The magnetic flux distribution can be regarded as sinusoidal.

B. Controller settings

A general purpose three-phase voltage inverter was used. The inverter was equipped with an intelligent power module PS21767 (Mitsubishi Electric Corp.).

The digital control system (PE-Expert III) was assembled by Myway Plus Corp. The controller was equipped with a TMS320C6713-225 (Texas Instruments) digital processor. Because the ripple current prediction and repetitive control algorithm require a rather rigorous calculation, we used a PWM carrier frequency of 1.25 kHz. If the carrier frequency is 2.5 kHz, it will be impossible to complete the process in half the carrier period.

The controller parameters are summarized in Table III. The listed controller parameters correspond to the parameters in the block diagrams shown in Figs. 3 and 17. Because the pole of the rotor position estimation was set to 500/3 rad/s as given in (14), the pole of the speed control loop was set to 100 rad/s.

In this method, an accurate and wide frequency band current sensor can be effective for detecting the signal current. In addition, the offset of the current sensor must be eliminated as much as possible before normal operation.

C. Steady-state characteristics

The steady state characteristics were evaluated experimentally. In the experiment, the rotating speed command was set to 50 min^{-1} (2.5 Hz of the electric output voltage

Table III Parameters of the Controller

PWM Carrier frequency	1250	Hz	$k_{p\omega}$	0.4	
Interrupt and sampling timings	double edges of the carrier		$k_{i\omega}$	2	
$k_{p\gamma}$	3.87		ω_{sc}	100	rad/s
$k_{i\gamma}$	70.75		k_{prep}	0.5	
$k_{p\delta}$	4.91		k_{irep}	100	
$k_{i\delta}$	70.75		V_{dc}	300	V

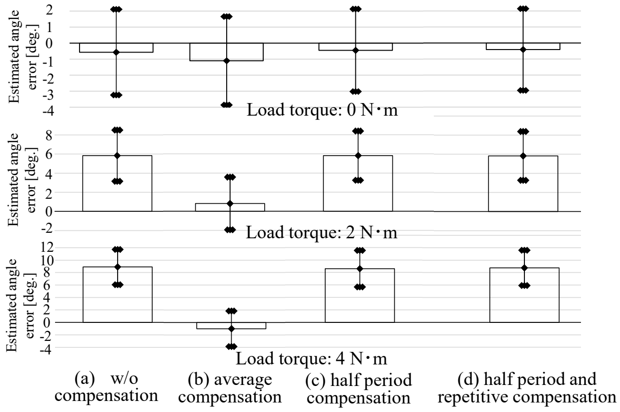

Fig. 19. Estimated steady state angle error with respect to the output voltage compensation method at a signal voltage of 50 V and rotating speed of 50 min^{-1}.

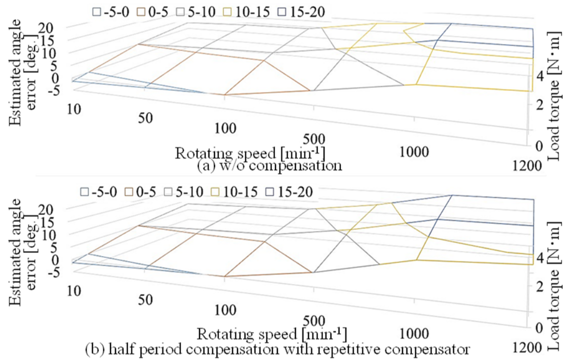

Fig. 20. Steady state estimated angle error characteristics with respect to the rotating speed and load torque; (a) without compensation, and (b) with the proposed half period compensation with the repetitive compensator.

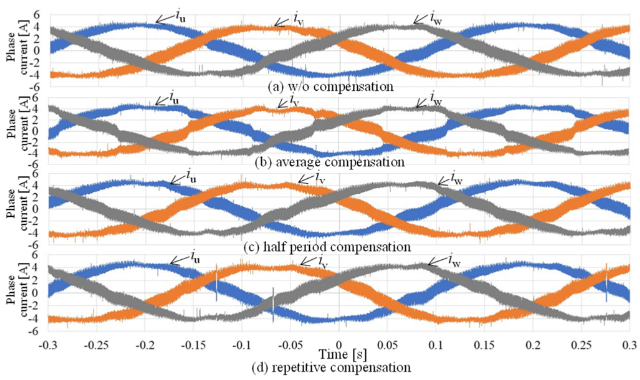

Fig. 21. Waveforms of the phase currents obtained from experiment at an injection voltage of 50 V; the load torque is 4 N·m and the rotating speed is 50 min^{-1}. (a) Without compensation, (b) with average voltage error compensation, (c) with carrier half period voltage error compensation, (d) with half period compensation and repetitive compensation.

frequency). The amplitude of the injected signal voltage was set to 50 V. For the test motor, the amplitude of the signal voltage is slightly larger than the minimum required value. The large amplitude of the signal voltage was set to demonstrate the effectiveness of the proposed output voltage error compensation method.

Fig. 19 shows the estimated average steady state angle error in one electric fundamental wave period for the different output voltage compensation methods when the magnitude of the load torque was changed. The error bar indicates one standard deviation from the average value. The compensation methods are as follows: (a) without compensation, (b) conventional average output voltage error compensation in the PWM carrier period, (c) proposed output voltage error compensation at every half period of the PWM carrier wave, and (d) proposed half period compensation method with repetitive current compensation. The estimated rotor angle error is less compared with those of other methods. In addition, the estimated angle errors of the other three compensation methods are almost the same. The error in the average compensation method (b) is small. However, desynchronization occurred during heavy load operation in method (b). Moreover, method (b) shows that an increase in the load torque does not affect the estimation angle error, which is different from the other cases. The average method (b) produced a sudden current change, as shown in Fig. 22. This represents a sudden change in the stator flux. This sudden change produces a torque change, which can lead to desynchronization under heavy loads.

Fig.20 shows the characteristics of the estimation angle error with the rotating speed and load torque. Fig.20(a) shows the case without compensation, and Fig.20(b) shows the case with the proposed half period compensation and repetitive current compensation. The two cases are almost identical. The error increased with an increase in the speed. In addition, the error increased with an increase in load torque. Note that magnetic saturation was not considered in the control method. When a large load torque is applied, magnetic flux density saturation may occur. This can cause the estimation angle error and angle error to be almost identical.

Fig.21 shows the stator current waveforms at steady state. Each compensation method described above was implemented, and the current waveforms were obtained. Current waveform distortion occurred in all cases at approximately zero ampere. Fig.22 shows the sampled stator current waveforms when the waveforms shown in Fig.21 were obtained. Fig.22(b) shows a discontinuous change in the sampled current at approximately zero ampere. The average compensation failed owing to failure to identify the actual current polarity. Fig.23 shows the estimated instantaneous current value at the instance of switching at a load torque of 4 N·m. The figure validates the ripple current model in (33) and (34) based on the experimental results. The estimation accuracy is reasonable at a large ripple current amplitude. When the ripple current is small, the signal voltage component is small in the corresponding phase, which can lead to an estimation error. The estimation error is mainly caused by current decay after switching. This phenomenon is particularly severe at a small average current. Fig. 24 shows the waveforms of the modulation indices obtained from experiment at an injection voltage of 50 V, load torque of 4 N·m, and rotating speed of 50 min^{-1}. Fig. 24(c) and (d) show that a smooth sinusoidal average modulation index m_{u_avrg} was obtained. This validates the use of the proposed half period compensation for reducing distortions in the command voltages. Fourier series expansion of the current waveforms of the four cases was performed, as shown in Fig. 25. The values were normalized using the fundamental wave current amplitude. The total harmonic distortions (THD) which take the harmonics up to the 50th order of the fundamental wave is summarized in Table IV. The THD of the proposed half period compensation with repetitive control is small with a value of 4.64 %. However, without the output voltage error compensation, the THD is 5.01 %. For the method without repetitive control, namely method (c), the THD is slightly lower at 4.54 %. This result

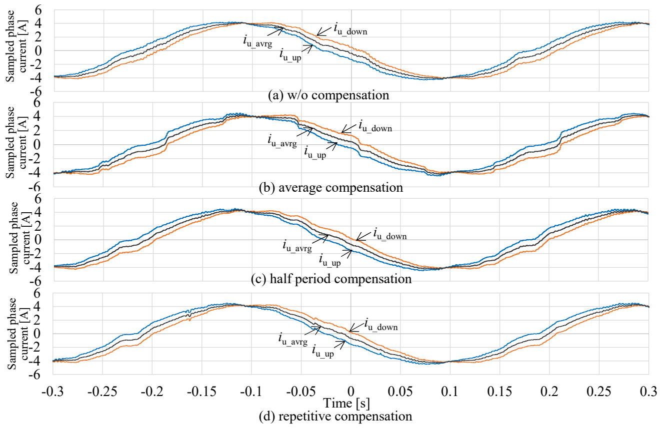

Fig. 22. Waveforms of the sampled phase currents obtained from experiment at an injection voltage of 50 V; the load torque is 4 N·m and the rotating speed is 50 min^{-1}.

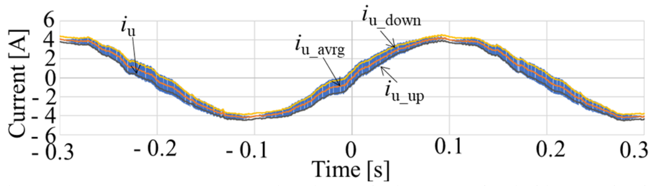

Fig. 23. Instantaneous current estimation at the instance of switching at a load torque of 4 N·m.

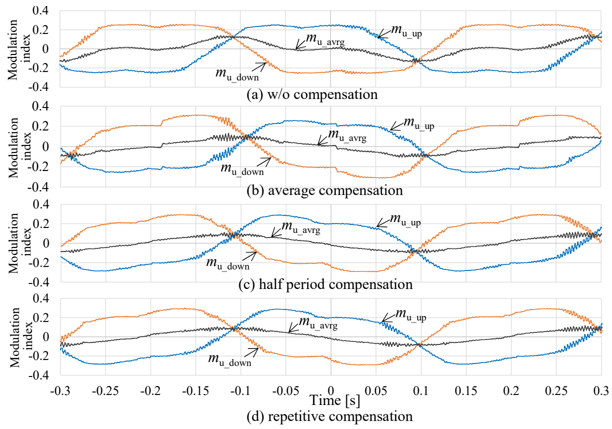

Fig. 24. Waveforms of the modulation indices obtained from experiment at an injection voltage of 50 V; the load torque is 4 N·m, and the rotating speed is 50 min^{-1}.

indicates that the proposed output voltage compensation reduces the current distortion even when there is a large current ripple in the sampled current.

In addition, the same frequency analysis was performed on the line-to-line output voltage waveforms shown in Fig. 26. The figure shows that the THD of the method without compensation was the smallest. The THD of the conventional average compensation was the largest. These results demonstrate that when output voltage compensation is performed under a large current ripple, the performance of the proposed output voltage compensation is superior to that of the conventional average compensation.

The high-frequency signal voltage injection method relies on the differential inductance, and the estimated angle converges to the angle with the least differential inductance. Therefore, when the differential inductance changes, particularly when the load is large, local magnetic field density saturation may occur, as illustrated in Fig. 27. This generates the estimation angle error [31][32] leading by the d-axis, which is true for the experimental results shown in Figs. 19 and 20.

The quality of speed control obtained using the proposed compensation method is shown in Fig. 28. The speed command was 50 min^{-1}. Fig. 28(a) shows the waveforms when no mechanical load was applied. Speed ripple occurred, but the ripple amplitude was small and the average speed coincided with its command. Therefore, the quality of speed control is reasonable. Fig. 28(b) and (c) show the waveforms at load torque values of 2 N·m and 4 N·m, respectively. In both cases, the average speed agreed well with the speed command despite the typical speed ripple.

D. Transient characteristics

The transient characteristics were examined to validate the proposed output voltage compensation method (d) when the signal voltage injection method was used. Fig. 29 shows the speed and rotor angle waveforms for a stepwise change in the speed command. In this experiment, the signal voltage is 50 V, the load torque is 4 N·m, and the positive torque direction is opposite the positive rotating speed. The speed command changed from -50 min^{-1} to 50 min^{-1}, as shown in Fig. 29(a) and from 50 min^{-1} to -50 min^{-1}, as shown in Fig. 29(b). These figures indicate that the actual speed followed the speed command within 60 PWM carrier periods (50 ms). The estimated rotor angle $\theta_{\gamma\delta}$ followed the encoder angle θ_r successively in both cases.

VI. Conclusion

This paper proposed an output voltage compensation method at each half period of a PWM carrier wave suitable for the carrier-synchronized signal voltage injection method. The proposed method measures the output voltage error in half the PWM carrier period. In addition, a method for estimating ripple currents was established for the signal voltage injection method. A repetitive current controller was combined with the proposed method to increase the robustness of the motor parameter variation. The experimental results show that the proposed method reduces the low-order current distortion and modulation indices even when the output current has a large current ripple. An assessment of the effect of magnetic saturation on the proposed method will form part of our future work.

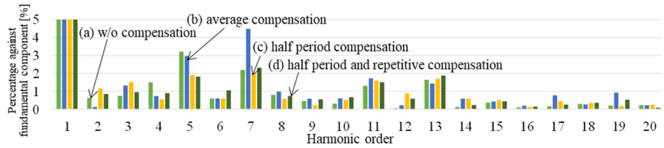

Fig. 25. Frequency analysis of the output current at an injection voltage of 50 V, rotating speed of 50 min^{-1}, and load torque of 4 N·m .

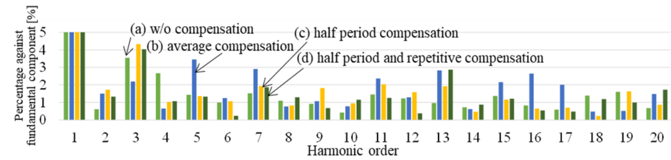

Fig. 26. Frequency analysis of the output line-to-line voltage at an injection voltage of 50 V, rotating speed of 50 min^{-1}, and load torque of 4 N·m.

TABLE IV THD OF THE OUTPUT VOLTAGE AND CURRENT

	Output current [%]	Output voltage [%]
(a) w/o compensation	5.01	8.61
(b) average compensation	6.59	10.63
(c) half period compensation	4.54	9.19
(d) half period and repetitive compensation	4.64	9.05

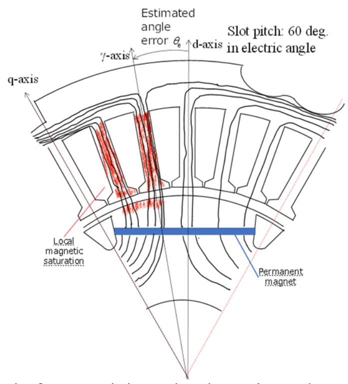

Fig. 27. Scheamatic for examining why the estimated angle error increases with the increase in the load torque magnitude .

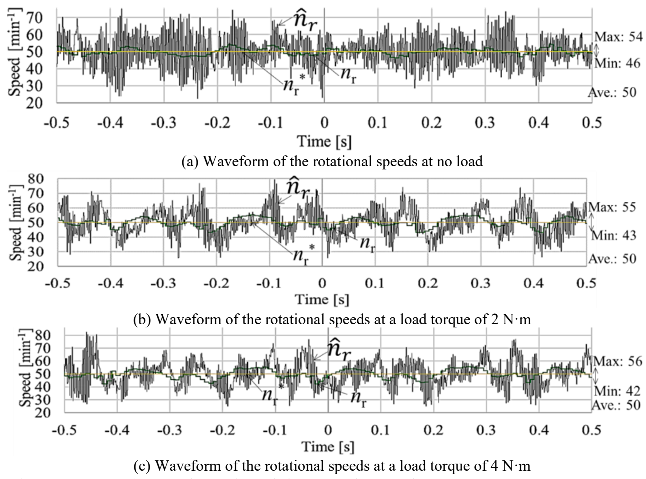

Fig. 28. Experimental results of the speed waveforms.

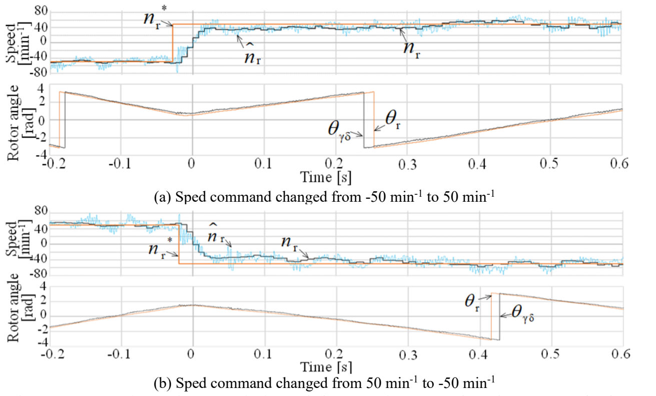

Fig. 29. Transient characteristics of the rotating speed and rotor angle for a stepwise change in the speed command.

ACKNOWLEDGMENT

The authors would like to thank Dr. Yoichi Hayashi, the President of Aoyama Motor Drive Technology, Japan, for providing useful suggestion. This work was carried out with the cooperation of Mr. Aaron Muam, a graduate student at the Nagasaki University. This work was supported in part by the Japan Power Academy Research Grant from 2018 to 2020.

REFERENCES

[1] S. Sul and S. Kim, "Sensorless control of IPMSM: Past, present, and future," *IEEJ J. Ind. Appl.*, vol. 1, no. 1, pp. 15–23, July 2012.

[2] Y. Kwon, J. Lee, and S. Sul, "Recent advances in sensorless drive of interior permanent-magnet motor based on pulsating signal injection," *IEEE Trans. Emerg. Sel. Topics Power Electron*., vol. 9, no. 6, pp. 6577–6588, 2021.

[3] R. Masaki, S. kaneko, M. Hombu, T. Sawada, and S. Yoshihara, "Development of a position sensorless control system on an electric vehicle driven by a permanent magnet synchronous motor," in *Proc. Power Conversion Conference,* Osaka, Japan, 2002.

[4] S. Murakami, T. Shiota, M. Ohto, K. Ide, and M. Hisatsune, "Encoderless servo drive with adequately designed IPMSM for pulse-voltage-injection-based position detection," *IEEE Trans. Ind. Appl*., vol. 48, no. 6, pp. 1922–1930, 2012.

[5] S. Kim, J. Ha, and S. Sul, "PWM switching frequency signal injection sensorless method in IPMSM," *IEEE Trans. Ind. Appl*., vol. 48, no. 5, pp. 1576–1587, 2012.

[6] C. Choi and J. Seok, "Compensation of zero-current clamping effects in high-frequency-signal-injection-based sensorless PM motor drives," *IEEE Trans. Ind. Appl*., vol. 43, no. 5, pp. 1258–1265, 2007.

[7] D. Kim, Y. Kwon, S. Sul, and R. Yu, "Suppression of injection voltage disturbance for high-frequency square-wave injection sensorless drive with regulation of induced high-frequency current ripple," *IEEE Trans. Ind. Appl*., vol. 52, no. 1, pp. 302–312, 2016.

[8] R, Raute, C. Caruana, C. Staines, J. Sumner, and G. Ascher, "Analysis and compensation of inverter nonlinearity effect on a sensorless PMSM drive at very low and zero speed operation," *IEEE Trans. Ind. Electron.*, vol. 57, no. 12, pp. 4065–4074, 2010.

[9] L. Gong and Z. Zhu, "A novel method for compensating inverter nonlinearity effects in carrier signal injection-based sensorless control from positive-sequence carrier current distortion," *IEEE Trans. Ind. Appl.*, vol. 47, no. 3, pp. 1283–1292, 2011.

[10] J. Guerrero, M. Leetmaa, F. Briz, A. Zamarron, and R. Lorenz, "Inverter nonlinearity effects in high-frequency signal-injection-based sensorless control methods," *IEEE Trans. Ind. Appl*., vol. 41, no. 2, pp. 618–626, 2005.

[11] T. Daido, R. Hisamatsu, T. Araki, and S. Hamasaki, "A consideration of the estimated position error of an IPMSM by PWM carrier synchronized voltage injection method," in *Proc. 24th Int. Conf. on Electrical Machines and Systems*, Korea, pp. 126–131, 2021.

[12] D. Leggate and R. J. Kerkman, "Pulse-based dead-time compensator for PWM voltage inverters," *IEEE Trans. Ind. Electron*., vol. 44, no. 2, pp. 191–197, 1997.

[13] T. Daido and Y. Hayashi, "Output voltage error compensation for every half of a carrier period in a voltage source inverter," *IEEJ J. Ind. Appl.*, vol. 8, no. 1, pp. 41–50, 2019.

[14] R. B. Sepe and J. H. Lang, "Inverter nonlinearities and discrete time vector current control," *IEEE Trans. Ind. Appl*., vol. 30, no. 1, pp. 62–70, 1994.

[15] N. Bedetti, S. Calligaro, and R. Petrella, "Self-commissioning of inverter dead-time compensation by multiple linear regression based on a physical model," *IEEE Trans. Ind. Appl*., vol. 51, no. 5, pp. 3954–3964, 2015.

[16] Y. Wang, W. Xie, X. Wang, and D. Gerling, "A precise voltage distortion compensation strategy for voltage source inverters," *IEEE Trans. Ind. Electron*., vol. 65, no. 1, pp. 59–66, 2018.

[17] J. Choi and S. Sul, "A new compensation strategy reducing voltage/current distortion in PWM VSI systems operating with low output voltages," *IEEE Trans. Ind. Appl*., vol. 31, no. 5, pp. 1001–1008, 1995.

[18] T. Mannen and H. Fujita, "Dead-time compensation method based on current ripple estimation," *IEEE Trans. Power Electron*., vol. 30, no. 7, pp. 4016–4024, 2015.

[19] N. Urasaki, T. Senjyu, K Uezato, and T. Funabashi, "An adaptive dead-time compensation strategy for voltage source inverter fed motor drive," *IEEE Trans. Power Electron*., vol. 20, no. 5, pp. 1150–1160, 2005.

[20] U. Abronzini, C. Attaianese, M. D'Arpino, M. Monaco, and G. Tomasso, "Steady-state dead-time compensation in VSI," *IEEE Trans. Ind. Electron*., vol. 63, no. 9, pp. 5858–5866, 2016.

[21] C. Choi and J. Seok, "Compensation of zero-current clamping effects in high-frequency-signal-injection-based sensorless PM motor drives," *IEEE Trans. Ind. Appl*., vol. 43, no. 5, pp. 1258–1265, 2007.

[22] T. Haneyoshi, A. Kawamura, and R. Hoft, "Waveform compensation of PWM inverter with cyclic fluctuating loads," *IEEE Trans. Ind. Appl*., vol. 24, no. 4, pp. 582–589, 1988.

[23] Z. Tang and B. Akin, "Suppression of dead-time distortion through revised repetitive controller in PMSM drives," *IEEE Trans. Energy Convers*, vol. 32, no. 3, pp. 918–930, Sept. 2017.

[24] Y. Inagaki, M. Mae, O. Shimizu, S. Nagai, H. Fujimoto, T. Miyajima, Y. Yasuda, and A. Yamagiwa, "Effect of harmonic current suppression on iron loss of IPMSM using repetitive perfect tracking control," *IEEJ J. Ind. Appl.*, vol. 2, no. 2, pp. 317–326, 2022.

[25] T. Zanma, M. Morimoto, and K. Yubai, "Suppression of harmonic current for IPMSM using generalized repetitive control," *IEEJ J. Ind/ Appl.*, vol. 3, no. 3, pp. 214–220. May 2014.

[26] A. Yoo, S. Sul, D. Lee, and C. Jun, "Novel speed and rotor position estimation strategy using a dual observer for low-resolution position sensors," *IEEE Trans. Power Electron.*, vol. 24, no. 12, pp. 2897–2906, 2009.

[27] S. Furutani, A. Satake, and T. Hozuki, "Inverter dead time compensation method using on-line tuning," *IEEJ J. Ind. Appl.*, vol. 10, no. 2, pp. 264–272, 2021.

[28] V. Blasko, "Analysis of a hybrid PWM based on modified space-vector and triangle-comparison method," *IEEE Trans. Ind. Appl*., vol. 33, no. 3, pp. 756–764, 1997.

[29] Z. Wang, Z. Cao, and Z. He, "Improved fast method of initial rotor position estimation for interior permanent magnet synchronous motor by symmetric pulse voltage injection," *IEEE Access*, vol. 8, pp. 59998–60007, 2020.

[30] T. Suzuki, M. Hasegawa, M Tomita, and S. Doki, "Initial position estimation for IPMSMs using comb filters and effects on various injected signal frequencies," *IEEJ J. Ind. Appl.*, vol. 4, no. 3, pp. 204–211, May 2015.

[31] Y. Kano and N. Matsui, "Rotor geometry design of saliency-based sensorless controlled distributed-winding IPMSM for hybrid electric vehicles," *IEEE Trans. Ind. Appl*., vol. 54, no. 3, pp. 2336–2348, 2018.

[32] K. Takeuchi, M. Matsushita, Y. Tuboi, and N. Ametani, "Identification method of current conditions suitable for synchronous machines having multiple operating points," *IEEJ J. Ind. Appl.*, vol. 10, no. 5, pp. 577–588, 2021.

Tetsuji Daido (Member, IEEE) received the B.E. degree in Electrical Engineering from Osaka City University, Japan in 2008 and the M.E. and Ph.D. degrees in Electrical Engineering from Osaka University, Japan, in 2010 and 2014, respectively.

From April 2014 to March 2018, he was a Research Associate at Aoyama Gakuin University, Japan. He has been with Nagasaki University, Japan, as a Research Associate since 2018. Currently, he has been engaged in rotating machine controls and semiconductor power converters.

He is a member of the IEEE and IEEJ.

Ryo Hisamatsu received the B.E. and M.E. degrees in Electrical Engineering from Nagasaki University, Nagasaki, Japan, in 2019 and 2021, respectively. His research interest is on the study of IPMSM drive using the high-frequency signal injection method.

Taisei Araki received the B.E. and M.E. degrees in Electrical Engineering from Nagasaki University, Nagasaki, Japan, in 2020 and 2022, respectively. His research interest is on the study of the inverter's output voltage compensation for IPMSM drive using the high-frequency signal injection method.

Shin-ichi Hamasaki (Member, IEEE) received the B.E., M.E., and Ph.D. degrees in Electrical Engineering from Yokohama National University, Kanagawa, Japan, in 1998, 2000, and 2003, respectively.

In 2003, he joined the Department of Electrical and Electronic Engineering, Nagasaki University, Nagasaki, Japan as a Research Associate. From 2007 to 2014, he was an Assistant Professor, and since 2015, he has been an Associate Professor in the Division of Electrical Engineering and Computer Science, Graduate School of Engineering, Nagasaki University. His research interests include control and application of multilevel converters, power conditioning systems, and machine drives.

He is a member of the IEEE Industry Applications, Industrial Electronics and Power Electronics Societies and a member of the IEEJ.